Development of cryogenic X-ray detectors based on Mo/Au TES

A. Camón

acamon@unizar.es

Instituto de Nanociencia y Materiales de Aragón (INMA), CSIC-Universidad de Zaragoza)

L. Fàbrega

Institut de Ciència de Materials de Barcelona (ICMAB-CSIC)

C. Pobes

Instituto de Nanociencia y Materiales de Aragón (INMA), CSIC-Universidad de Zaragoza)

P. Strichovanec

Instituto de Nanociencia y Materiales de Aragón (INMA), CSIC-Universidad de Zaragoza)

J. Bolea

Centro Universitario de la Defensa

J. I. Rico-Camacho

Instituto de Nanociencia y Materiales de Aragón (INMA), CSIC-Universidad de Zaragoza)

J. L. García-Palacios

Instituto de Nanociencia y Materiales de Aragón (INMA), CSIC-Universidad de Zaragoza)

Research Article

Keywords: Cryogenic Detectors, Superconductivity, Transition Edge Sensors

Posted Date: October 14th, 2025

DOI: https://doi.org/10.21203/rs.3.rs-7700799/v1

Additional Declarations: No competing interests reported.

Abstract

Transition Edge Sensors (TES) have emerged as highly sensitive radiation detectors with applications ranging from astrophysics to materials science. In the framework of the Athena X-ray mission, we have developed Mo/Au-based TES devices designed to meet the specifications defined by ESA. The detectors were fabricated using a Mo/Au/Au trilayer process and characterized in a dilution refrigerator using a SQUID readout. From I–V curves and complex impedance measurements, we extracted the electrothermal parameters of the TES, which are consistent with theoretical models. Noise spectra were analyzed to estimate the energy resolution, and an excess noise factor was obtained from the comparison of theoretical and experimental data. A spectral resolution of 3.5 eV was achieved for 5.9 keV X-rays from a ^{55}Fe source.

1. Introduction

Since K. D. Irwin proposed their use under voltage bias in 1995 [1], microcalorimeters based on Transition Edge Sensors (TES) have become one of the best radiation detectors available. Depending on the design and the absorber material used, they are able to detect individual photons across a wide range of frequencies, from microwaves to Gamma-rays, with exceptional spectral resolution [2]. Moreover, they exhibit extremely low dark count rates. TES devices are nowadays employed in a variety of fields, including astrophysics and materials science [3]. One notable upcoming application is the Athena mission [4], an X-ray space telescope to be launched by the European Space Agency (ESA) in the coming decade.

Our group has been developing TES devices with the demanding Athena specifications in mind for more than a decade. This has also opened the possibility for new applications in the same energy range (synchrotron facilities and axion searches). In this work, we summarize the main milestones obtained up to now. Section 2 describes the detector fabrication process, Section 3 outlines the characterization setup, and Section 4 presents some results for a representative device.

2. Fabrication

Four-inch silicon wafers with 500 nm thick low stress Si_3N_4 layer in both sides are used as substrate. To avoid problems associated with Mo oxidation when the sample is transferred between the sputtering system and the e-beam during the fabrication process, our group developed the trilayer solution [5], combining magnetron sputtering and e-beam deposition. We use a magnetron AJA Orion 5 UHV sputtering system and an E-Beam PVD system Edwards 500 UHV. First, the 45nm of Molybdenum layer is deposited using Radio Frequency (RF) power supply from a 2-inch diameter Mo target of 99.95% purity. Then, a 15 nm protective Au layer is deposited by direct current (DC) power supply from a 2-inch diameter Au target of 99.99% purity. The argon working pressure is fixed to 3 mTorr. The deposition rates are 9 nm/min for Mo and 10 nm/min for Au. Afterwards, the wafer is taken out from the sputtering and loaded into the e-beam evaporation system, where 250 nm of high purity (99.99%) gold is evaporated

(rate of 10 nm/min). These Mo and Au thicknesses determine a critical temperature close to 100 mK via the proximity effect [6].

After finishing the trilayer deposition, the Si_3N_4 membranes on the back side of wafer are defined by using optical lithography (K.Suss MA6 aligner) with positive photoresist AZ ECI 3027. The size of the aperture in the Si_3N_4 backside layer is calculated for anisotropic wet etching of (100) silicon in KOH solution to reach the correct size of membrane on the top side of the wafer. Then, Si_3N_4 is etched away by reactive ion etching (RIE) with SF_6 plasma.

Positive resin lithography (AZ ECI 3027) is used to define the area of the thermometer (Mo/Au). The combination of Ion Milling (IM) and RIE allows etching away the gold and partially the molybdenum layer, where approximately 10nm of Mo layer is left. After resin cleaning, 150 nm of Nb is deposited by DC sputtering with the rate 7.5 nm/min at a pressure 3 mTorr of Ar. Before Nb deposition the surface is cleaned by RF bias Ar plasma in the same chamber. This step allows to remove all surface contamination and produces a clean interface between Mo and Nb. Next, the Nb paths are defined with positive photoresist (AZ ECI 3027). The RIE (CF_6 plasma) is used to etch away the Nb and the rest of the Mo layer.

After removal of the remaining photoresist, a two-level lithography process is carried out for the fabrication of a cantilevered X-ray absorber. First, the positive photoresist (AZ ECI 3027) is used to define 2.5μm stems that support the absorber on the Si_3N_4 membrane, and produce a thermal contact point to the Mo/Au thermometer. Then, a Ti/Au (5/500 nm) seed layer is evaporated on, forming a bottom contact for plating. The area of absorber is defined by a second lithography using 7μm-thick positive photoresist (AZ XT10), being later exposed for plating.

A homemade electrochemical cell (EC) supplied by an AUTOLAB PGSTAT12 potentiostat is used for gold plating. This method permits deposition of high purity gold (RRR = 35) of few micrometers thickness. Three-electrode system consists of a Platinum counter-electrode (CE), a Ag/AgCl reference electrode, and a working electrode (WE). The WE is the 4” wafer with the gold seed layer and chips distribution defined by lithography to open a total area of 10 cm^2. A commercial solution, TECHNI GOLD 25 ES is used for Au plating. The 2.5 μm gold layer is deposited by applying a constant current mode with the solution heated to 55˚C. The current is set to 1.2 mA/cm^2 providing a deposition rate of 75 nm/min, that allows depositing a bright and flat Au gold layer. In some cases, to increase the quantum efficiency of the absorber, a Bi layer is deposited using another commercial plating solution, NB 100 (NB Technologies). A constant current of 2.5 mA/cm^2 at room temperature provides a deposition rate of approximately 80 nm/min. The typical Bi thickness achieved is between 3 to 5 μm.

After cleaning the upper thick photoresist, the seed layer is etched off by IM. Finally, the bottom photoresist is dissolved and cleaned by acetone, isopropanol and ethanol bath. To release the Si_3N_4 membranes, the Si substrate is wet etched selectively by 40% KOH solution at 80˚C. To protect the top

side of the wafer, where the TES are, the wafer is hermetically closed into the PEEK wafer chuck, and only the backside of the wafer is exposed for wet etching.

Up to 32 (10 x10 mm) chips are usually distributed in every 4” wafer. This allows for a wide variety of designs to be tested, from bilayer geometry or absorber coupling in single pixels, to arrays. Figure 1 shows a schematic cross-section of a typical single pixel.

TES devices with different geometries, sizes, and absorber stem position have been designed and fabricated. An example of a representative TES, developed to achieve the best energy resolution in accordance with the specifications of the X-IFU instrument of the ATHENA mission, is presented in Fig. 2.

3. Characterization setup

Figure 3 shows a schematic of the circuit used for the TES. When a photon is absorbed, the TES heats up, and since it is biased within the superconducting transition, its resistance changes sharply. This leads to a change in the current flowing through the SQUID's pickup coil. The SQUID detects this variation and converts it into a voltage pulse. The SQUID used is a dual-channel model C6_X226LB provided by PTB (Berlin). It also includes the shunt resistor (R_{shunt}), which in our case is 2 mΩ. An encapsulated ^{55}Fe source, mounted directly above the TES, is eventually used as the X-ray source. The full setup is hosted in a Bluefors dilution refrigerator, achieving a base temperature below 10 mK.

TESs are highly sensitive to magnetic fields. For this reason, the entire holder is magnetically shielded using a superconducting aluminum enclosure and a CRYOPERM shield. If any residual field remains, B_{res}, it is compensated by using a superconducting Helmholtz coil placed at the sample holder, ensuring that the TES operates in a nearly zero-field environment. The residual field may vary between measurements, with typical values up to 10 μT. To estimate B_{res}, we bias the TES within its transition region and sweep the applied magnetic field to maximize the SQUID output.

To minimize external noise, the mains are filtered through an ultra-isolation transformer and an uninterruptible power supply (UPS). To avoid ground loops, optical fiber connections are used. A low-noise differential preamplifier (Stanford Research Systems SR560) is used to set the bandwidth and conditioning the signal from the SQUID. Finally, a 24-bit NI PXI-5922 digitizer is used to acquire voltage pulses generated by the arrival of X-ray photons at the detector.

By using this setup, several measurements are performed to fully characterize the detector. I-V curves are acquired with a HP 3458A multimeter at different bath temperatures, T_{bath} (Fig. 4), from which the TES thermal parameters are extracted (n, K, T_0, and G) [7]. A Hewlett-Packard HP 3562A spectrum analyzer is used to perform complex impedance measurements [8] (Fig. 5). Based on a one thermal block model (1TB) [9], we estimate the electrical parameters: α, β (logarithmic derivatives of R(T)), the effective τ_I, and heat capacity C. The noise performance parameters are also estimated [9].

4. Results

The characterization results of a representative TES are presented below. Assuming that in a 1TB model P_{bath} = P_{joule}, by fitting the set of I–V curves at different bath temperatures to the expression

$$P_{bath} = K(T^n - T_{bath}^n)$$

the thermal parameters of the TES (n, K, G, and T_0) are obtained, as summarized in Table 1. The n value of 3.5, is in good agreement with the calculations reported by Anghel et at. [10]

Table 1
Different TES parameters measured at 20% of Rn

Lenght	**80 um**
Width	40 um
T_0	93 mK
Rn	57 mΩ
n	3,5
G	156 pW/K
C	1.5 pJ/K
α	300
β	4
L	57 nH
τ_I	145 us

Electrical parameters of the TES (α, β, τ_I and C) are derived by fitting the complex impedance data at different bias points to a 1TB model [9] (seeTable 1).

The TES energy resolution can be estimated from the experimental noise spectrum (ΔE_{exp}) and also from the theoretical noise spectrum (ΔE_{th}), both based on the noise model (Fig. 6–7).

In both cases, the definition follows Eq. (97) from [9] although the integral bandwidth is restricted between 10 Hz and 100 KHz.

$$\Delta E_{FWHM} = \frac{2\sqrt{2Ln(2)}}{\sqrt{\int_0^\infty \frac{4}{NEP(\omega)^2} d\omega}}$$

From the difference between the theoretical and experimental noise, the excess noise parameter M^2 is estimated (Fig. 8). The figure shows the relationship between M^2 and α, which remains approximately constant [11] for this device. A detailed analysis of the relationship between M^2 and the logarithmic derivatives for different TESs is presented elsewhere. This relation implies that TES with a larger α do not necessarily achieve better energy resolution, as it is often associated with higher M^2 values. Therefore, a trade-off between both parameters is required.

Finally, Fig. 9 shows a histogram from the acquisition of 1730 pulses, yielding a final spectral resolution (ΔE_{final}) of 3.5 eV for the Ka complex of the ^{55}Fe source (5.9 keV). The discrepancy between ΔE_{final} and ΔE_{exp} suggests that probably, the intrinsic resolution of the devices is already at the state of the art and that the measured resolution is being limited by a set-up contribution. We are working on improving temperature stability and vibration isolation to reduce this contribution. A detailed analysis of the effect of T_{bath} on the resolution at low operating point will be presented elsewhere.

5. Conclusions and Outlook

We are developing Mo/Au-based TES X-ray detectors, focusing on the specifications defined by ESA for the X-IFU instrument of the Athena mission. We have developed fabrication and full characterization setups, and have designed, fabricated and characterized many devices. In this paper we presented the results achieved so far. Energy resolutions of 3.5 eV have been obtained, possibly limited by experimental setup contributions. Further improvements are currently being implemented, including temperature stability better than 1 μK and a new anti-vibration system. These upgrades are expected to enable further enhancement of the achieved energy resolution.

Although this manuscript presents only the results of a representative TES for X-IFU, different TES have been developed in order to perform a broad range of studies. For instance, in [12] the physical origin of the superconducting transition was investigated; in [13] the temperature and current sensitivities of bare Mo/Au TES were analyzed; and in [14] the proximity effect in Mo/Au TES was explored.

Ongoing work is currently focused on the optimal choice of the operating point and on the influence of TES design on fundamental parameters and excess noise as well as on the development of TES for other applications.

Declarations

The authors have no relevant financial or non-financial interests to disclose

The data that support these findings are available from the corresponding author upon reasonable request.

Author Contribution

A.C. wrote the main manuscript text and prepared figures 4-8. P.S. prepared figures 1-2. J.I.R. prepared figure 3. C. P. prepared figure 9. All authors reviewed the manuscript.

Acknowledgments

The Spanish ”Ministerio de Ciencia, Innovación y Universidades” supports and funds this works, MICIU/AEI/10.13039/501100011033 under Grants No. PID2021-122955OB-C42 (also funded by FEDER, UE), No. PID2024-155779OB-C32, No. CEX2023-001286-S (Severo Ochoa Centers of Excellence). We also acknowledge the Aragón Regional Government through project QMAD (E09 23R). LF acknowledges also Spanish MICINN for support through the Severo Ochoa Programme for Centres of Excellence (project MATRANS42, CEX2023-001263-S). We also acknowledge PTB (Berlin) for providing us with excellent SQUIDs, and Jörn Beyer for his valuable help and advice.

Data Availability

The data that support these findings are available from the corresponding author upon reasonable request.

References

1. K.D. Irwin, Appl. Phys. Lett. **66**(15), 1998 (1995)
2. J.N. Ullom, D.A. Bennett, Supercond Sci. Technol. 28 no 8, 084003, (2015)
3. Appl, Sci, (2021) https://doi.org/10.3390/app11093793
4. D. Barret, V. Albouys, J.-W. den Herder, L. Piro et al., Exp. Astron. (2023). https://doi.org/10.1007/s10686-022-09880-7
5. L. Fàbrega, I. Fernandez, O. Gil, M. Parra, A. Camón, R. Gonzalez, J. Sese, F. Briones, IEEE Trans. Appl. Supercon. **19**(3), 460 (2009)
6. J.M. Martinis, G.C. Hilton, K.D. Irwin, Nucl. Instr Meth A, (444), 23 (2000)
7. T. Saab, E. Apodaca, S. Bandler, K. Boyce, J.A. Chevernak, E. Figueroa, F.M. Finkbeiner, M.J. Li, C.A. Kibourne, Nucl. Instr Meth A, (520), 281 (2004)
8. M.A. Lindeman, S. Bandler, R.G. Brekosly, J.A. Chevernak, E. Figueroa, F.M. Finkbeiner, M.J. Li, C.A. Kibourne, Rev. Sci. Instrum. **75**, 1283 (2004)
9. K.D.Irwin and G.C.Hilton, in Enss C. (eds.) Cryogenic Particle Detection, Topics in Appl. Phys. 99, Springer, Berlin Heidelberg, pp 63–150 (2005)
10. D.-V. Anghel, C. Caraiani, Y.M. Galperin, Phys. Scr. **94**(10), 105704 (2019)

11. N.A. Wakeham, J.S. Adams, S.R. Bandler, S. Beaumont, J.A. Chervenak et al., J. Appl. Phys. (2019). https://doi.org/10.1063/1.5086045
12. L. Fàbrega, A. Camón, C. Pobes, P. Strichovanec, J. Appl. Phys. (2024). https://doi.org/10.1063/5.0225871
13. L. Fàbrega, A. Camón, C. Pobes, P. Strichovanec, J. Bolea, M. Mas, J. Low Tem Phys. (2022). https://doi.org/10.1007/s10909-022-02721-0
14. L. Fàbrega, A. Camón, C. Pobes, P. Strichovanec, IEEE Trans. Appl. Supercon. (2019). https://doi.org/10.1109/TASC.2019.2903994

Figures

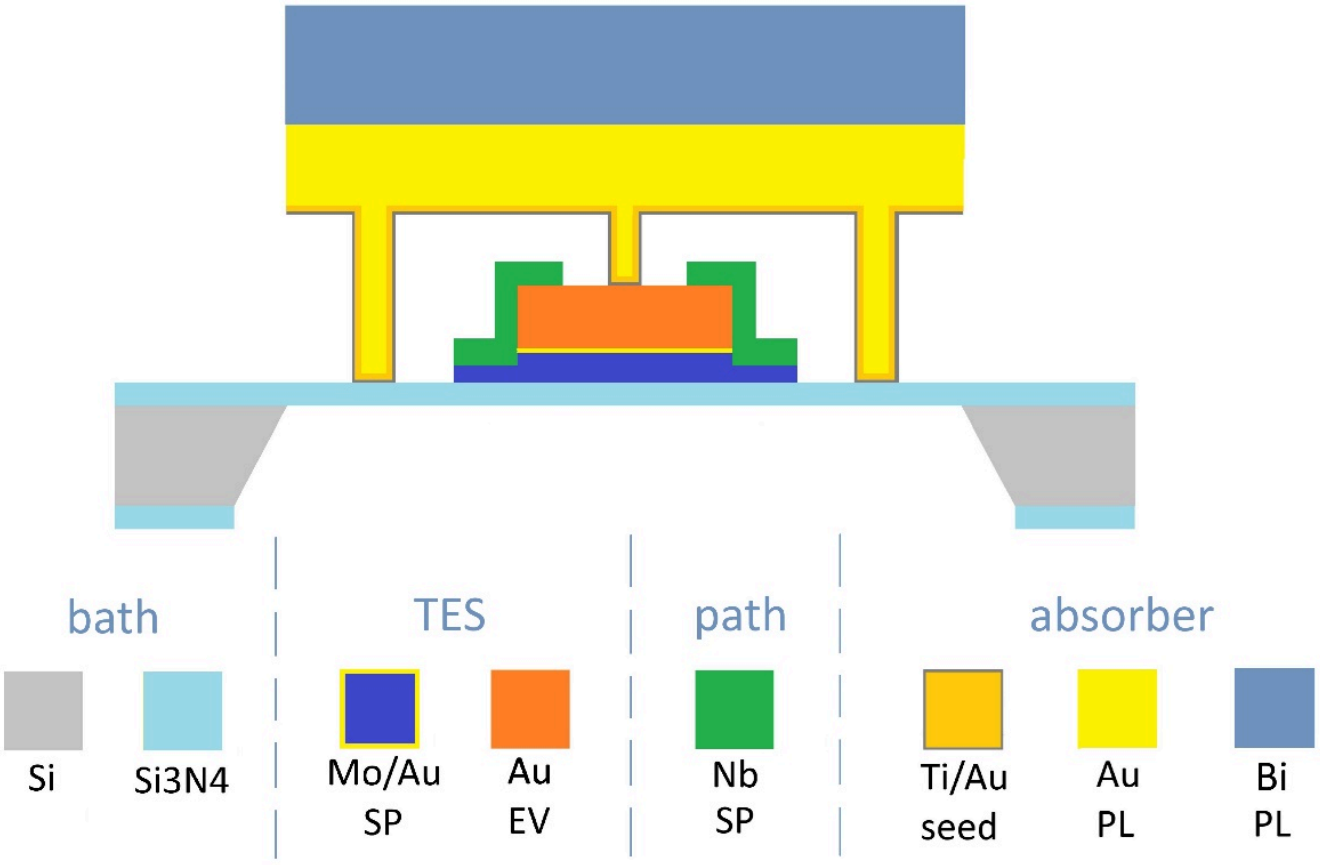

Figure 1

Schematic cross-section of a TES with absorber (SP: sputtering, EV: e-beam evaporation, PL: plating)

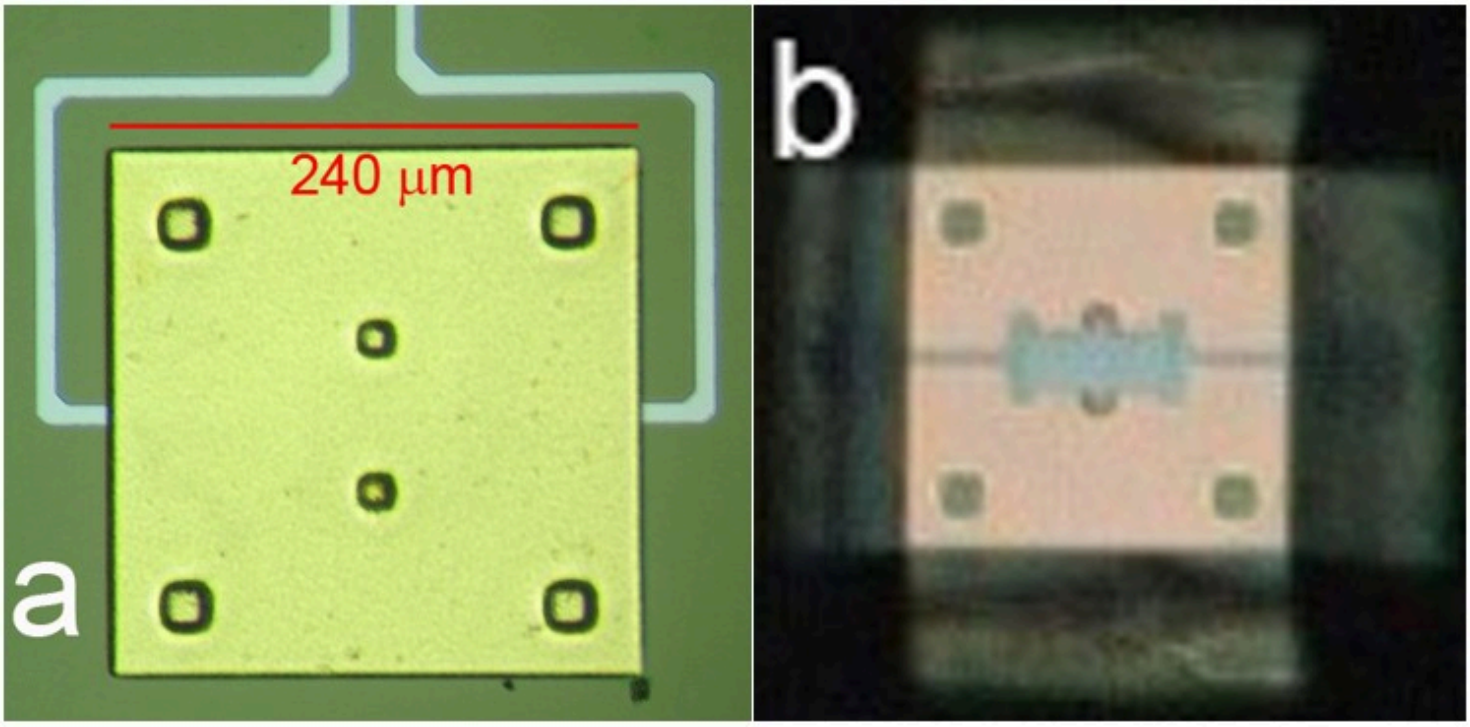

Figure 2

Optical micrographs of TES. (a) Top-view image of a TES showing the Au absorber (240 × 240 µm), two central stems tangent to the edge of the trilayer, and four outer stems laying on the membrane. Mo/Nb paths with a width of 15 µm can also be seen. (b) Bottom-view image of the same detector through the membrane, showing the TES sensor in addition to the absorber stems and the paths.

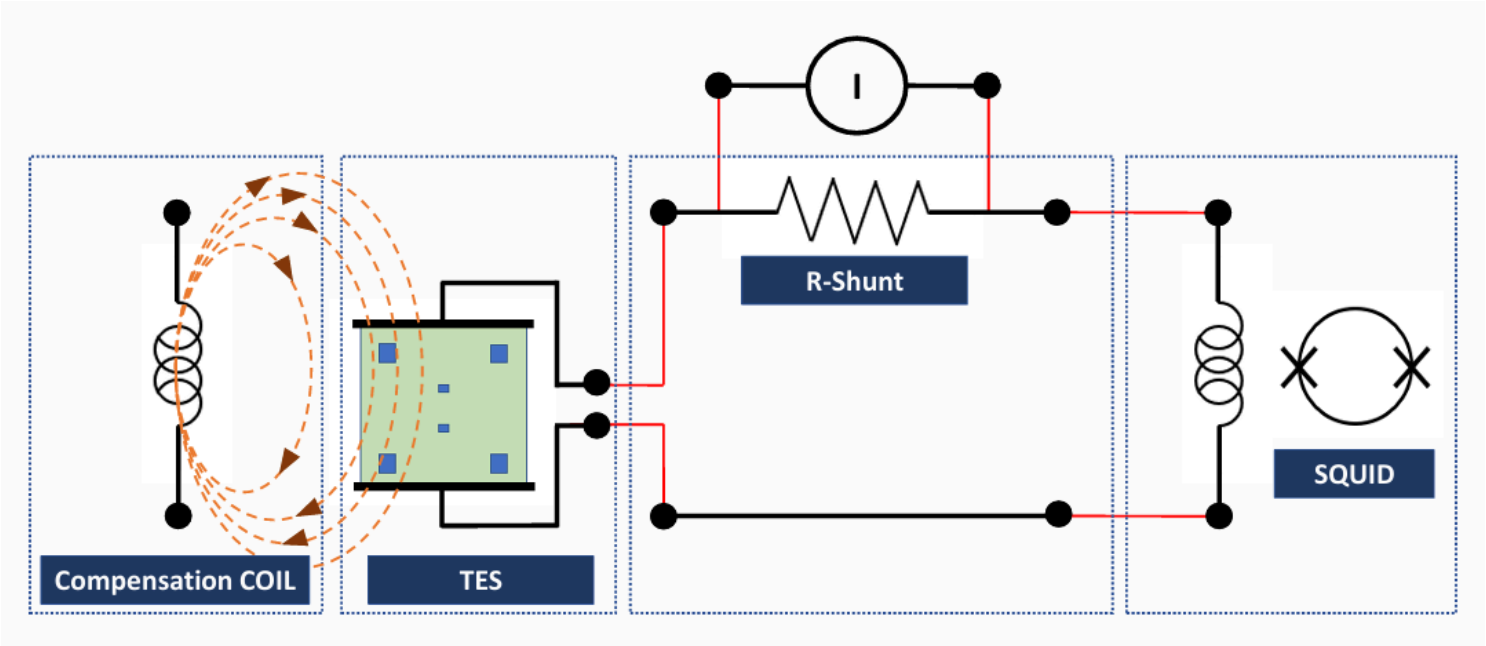

Figure 3

Scheme of the circuit used for the TES characterization.

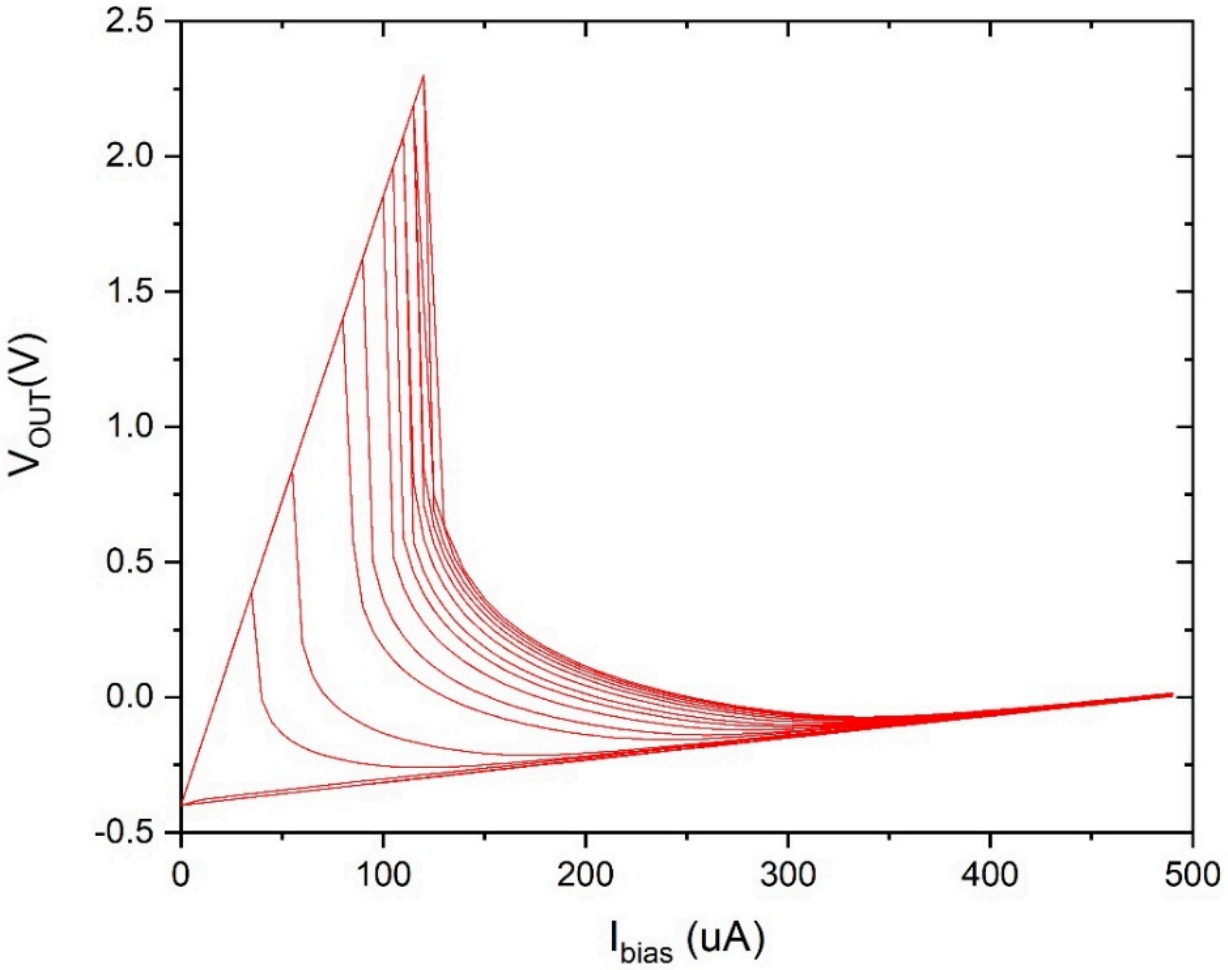

Figure 4

A set of I-V curves at different T_{bath}, from 40 mK to 150 mK (right to left)

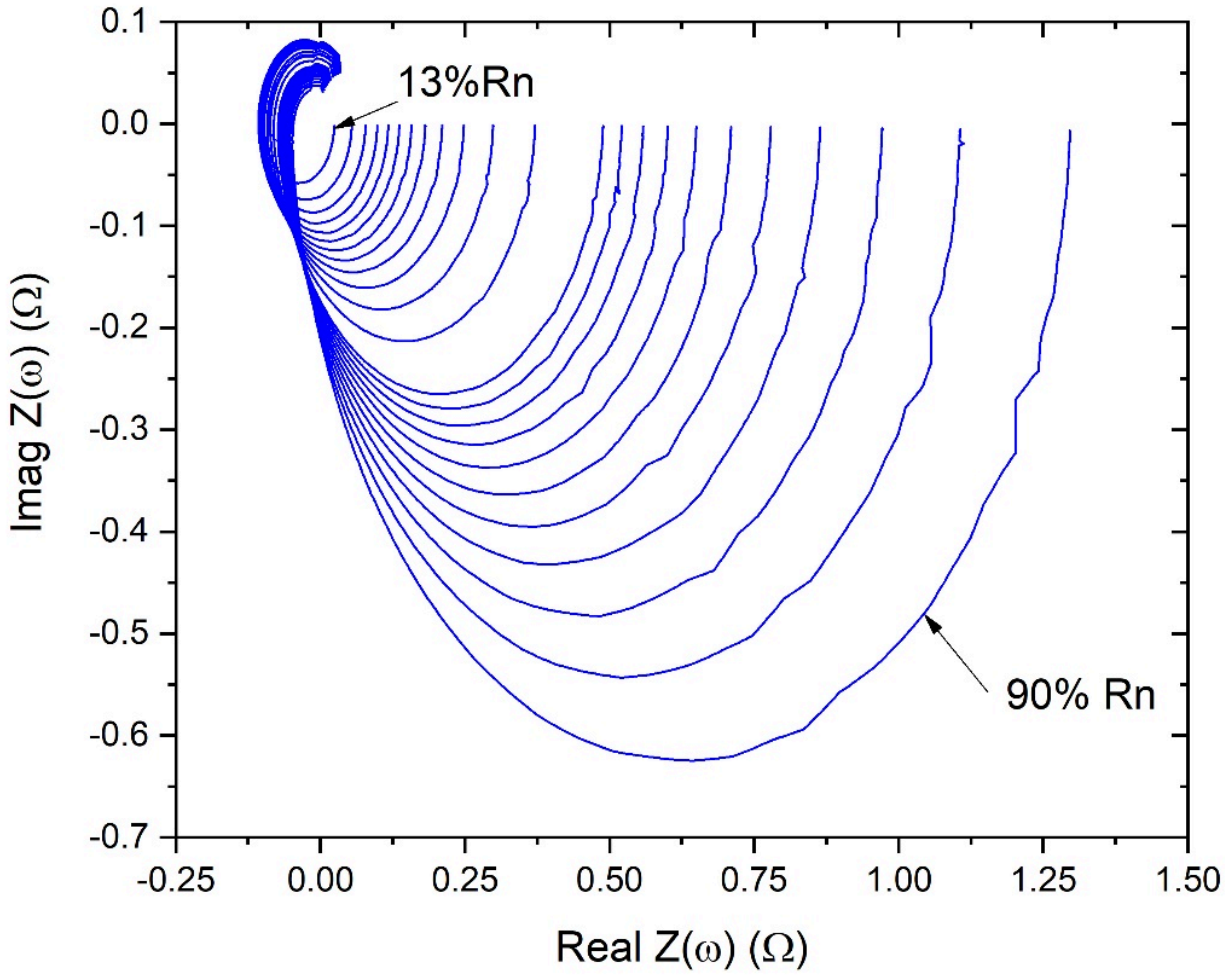

Figure 5

A set of Z(ω) curves at different operation points at T_{bath} = 50 mK.

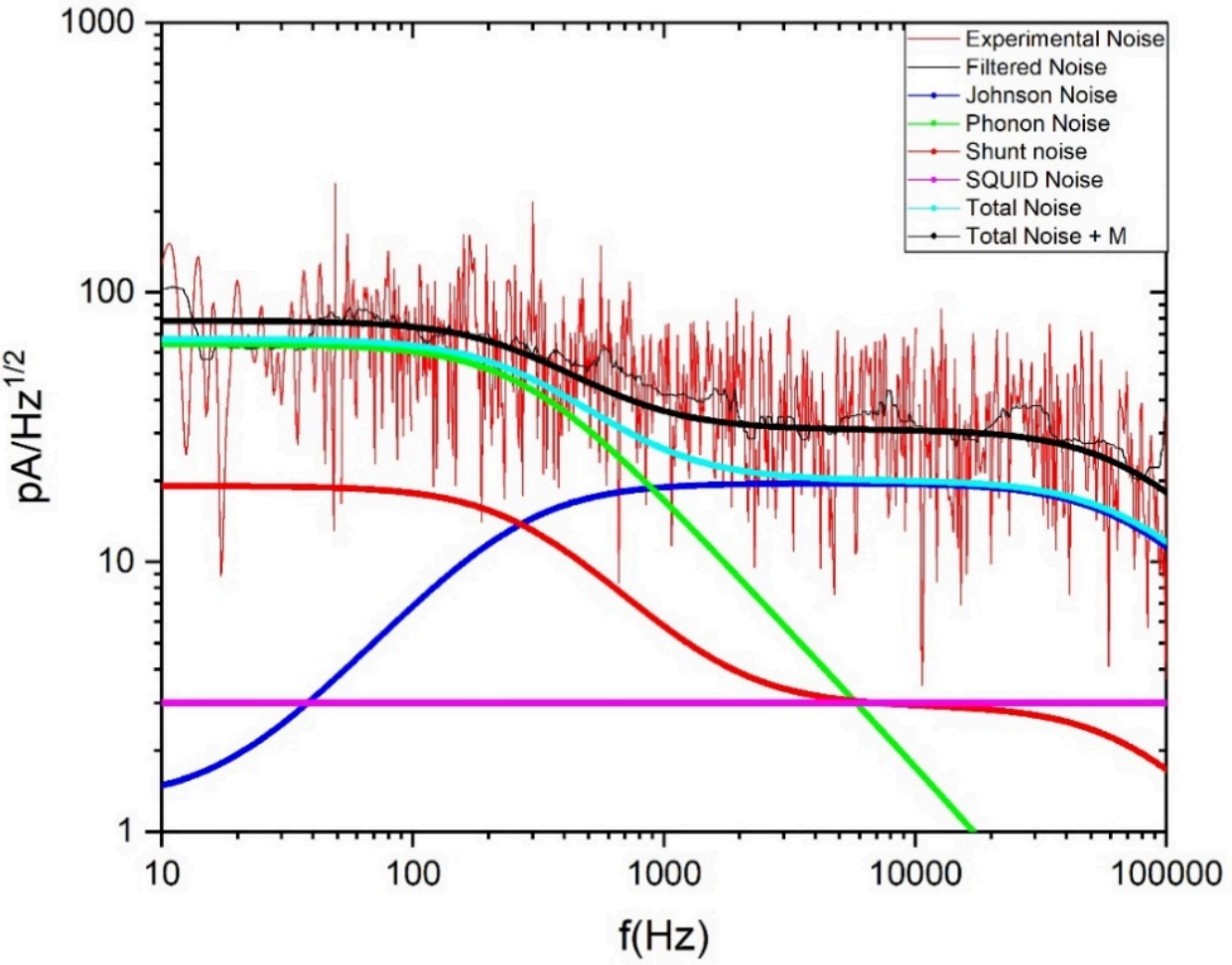

Figure 6

Experimental noise spectrum of the TES, along with the different noise contributions calculated using the TES parameters obtained from I-V curves and complex impedance using a 1TB model. Their sum defines the theoretical noise model (cyan line).

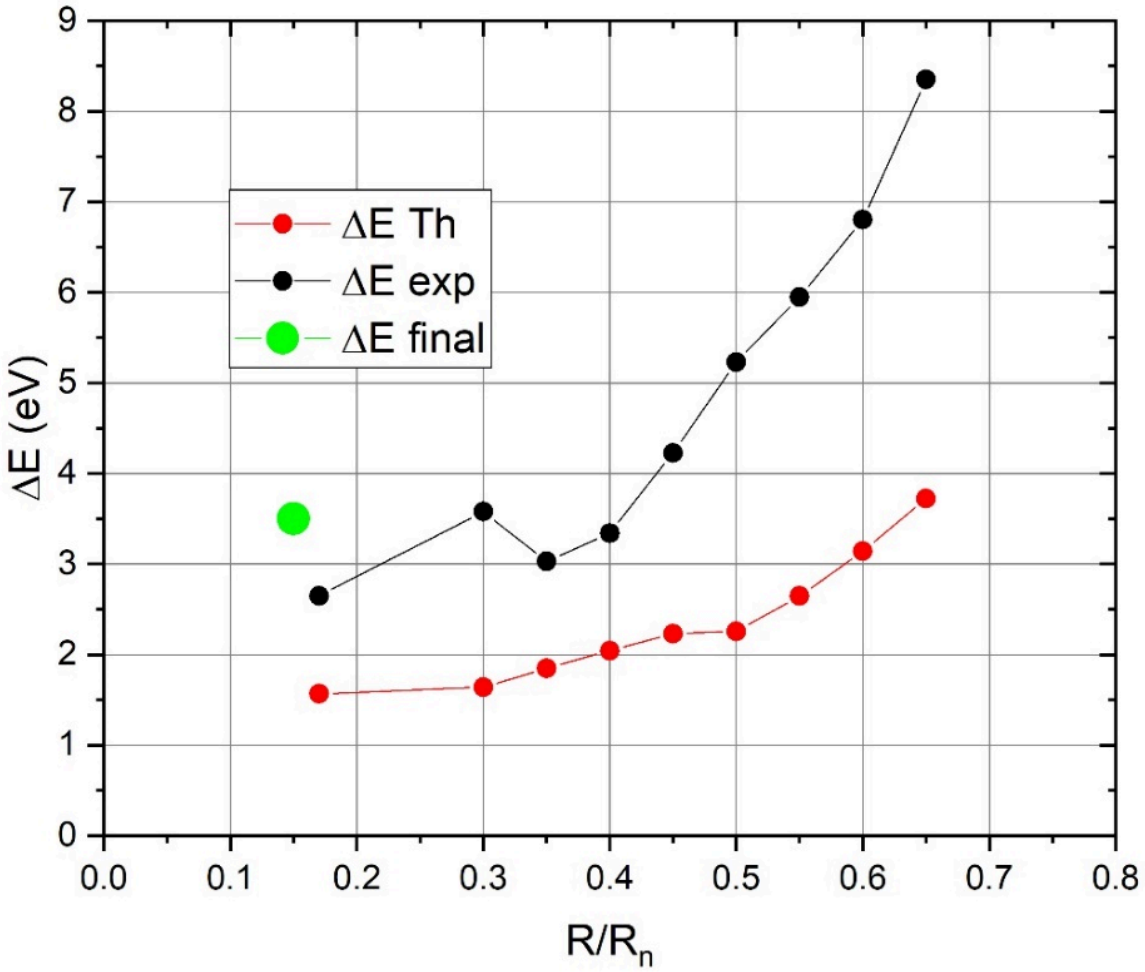

Figure 7

ΔE_{Th} and ΔE_{exp} as a function of R/Rn. For a typical operating point of 0.15, the ΔE_{Th} is approximately 1.5 eV, while the ΔE_{exp} is around 2.7 eV and ΔE_{final} is 3.5 eV.

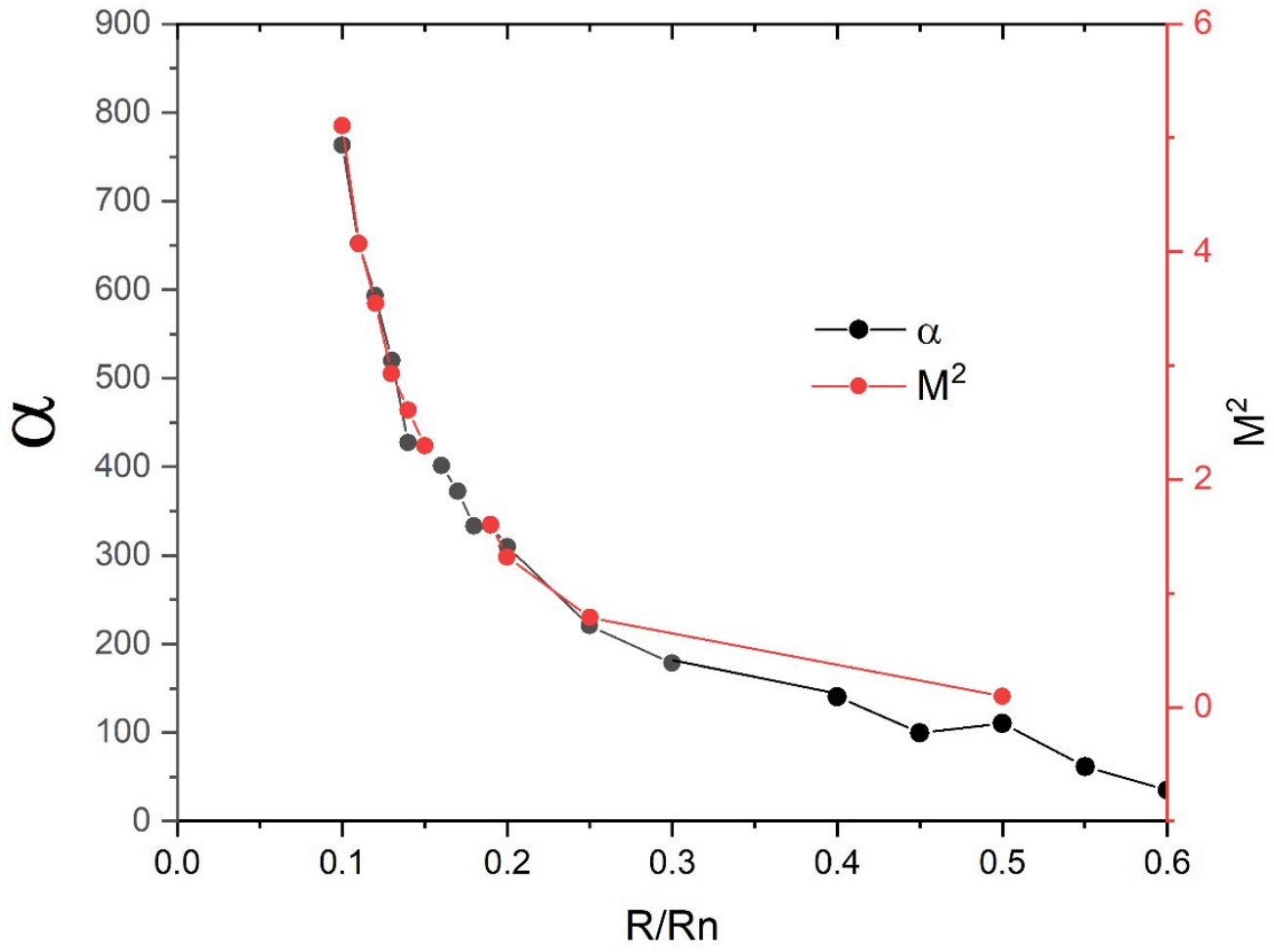

Figure 8

M^2 and α as a function of R/Rn

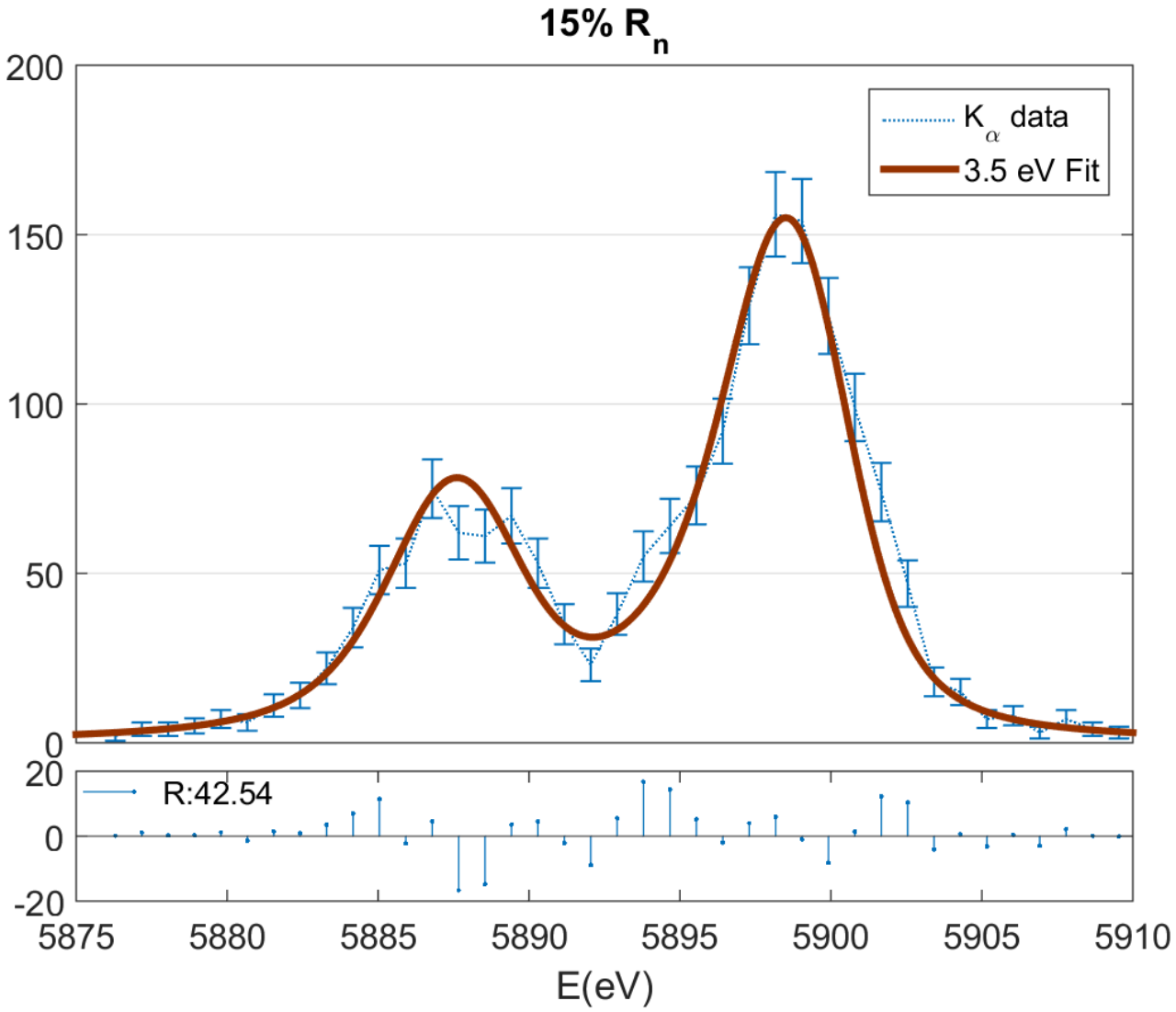

Figure 9

Spectrum of ^{55}Fe Ka lines obtained with the pixel in Fig. 2. at 15 % of Rn